



ELSEVIER

Contents lists available at ScienceDirect

Flow Measurement and Instrumentation

journal homepage: www.elsevier.com/locate/flowmeasinst

Capacitance wire mesh imaging of bubbly flows for offshore treatment applications



Gnouyaro P. Assima^a, Faiçal Larachi^{a,*}, Eckhard Schleicher^b, Markus Schubert^b

^a Department of Chemical Engineering, Université Laval, Québec, QC, Canada G1V 0A6

^b Helmholtz-Zentrum Dresden-Rossendorf, Institute of Fluid Dynamics, Bautzner Landstraße 400, 01328 Dresden, Germany

ARTICLE INFO

Article history:

Received 9 February 2015

Received in revised form

22 July 2015

Accepted 29 July 2015

Available online 31 July 2015

Keywords:

Bubble column

Wire mesh capacitance sensor

Gas holdup

Gas interstitial velocity

Swell simulator

Marine applications

ABSTRACT

The impact of ship motion on bubbly flow was emulated using a swell simulator to expose flow structure changes emerging in bubble columns relevant to offshore floating applications. Roll, roll + pitch, yaw, heave and sway were implemented at various frequencies and changes in bubbly flow resulting from the imposed motions were monitored for the first time by means of a dual capacitance wire mesh sensor to measure local gas holdup and velocity. Visualizations of the two-phase flow revealed that roll, roll + pitch, and high-frequency sway were the most impactful in terms of bubble zigzag and swirl, and bubble-clustering and segregation due to vessel dynamic inclinations. As a consequence of these motions, lateral migration of bubbles and their clustering enhanced liquid recirculation and local streamwise gas velocity. Compared to static vertical bubble column, bubbly flow pattern was barely altered by yaw and low-frequency sway except the heave displacements which tended to slowdown the bubble rise.

© 2015 Elsevier Ltd. All rights reserved.

1. Introduction

Three main types of multiphase reactors, namely, trickle beds, ebullated (or gas–liquid–solid fluidized) beds and (slurry) bubble columns, are commonly used in chemical, biochemical, petrochemical, and wastewater treatment operations [1]. Bubble columns imposed themselves as the simplest among them by being auspicious in accomplishing various processes such as petroleum residues conversion, hydrotreating, Fischer–Tropsch synthesis, coal liquefaction, hydrogenation, wastewater treatment [2–5] and so forth. Bubble columns as multiphase reactors are perceived to be particularly useful in fuel processing and gas treatment applications with regard to offshore oil and gas fields in deeper water and areas far off continental shores on account of an increasing scarcity of land-based hydrocarbon reserves [6]. Remoteness of oil and gas production sites is matter-of-factly imposing technology shifts in order to meet with specific offshore exploitation constraints [7]. Among the systems envisioned as viable options for deep-water/offshore fields, floating production storage and off-loading (FPSO) units are gaining momentum among industry players as they allow integration on the same floating systems of extraction, production and storage operations. Basically, FPSO units allow extracted hydrocarbons to be treated and refined on-site by means of onboard multiphase reactors [8].

Implementation of efficient (slurry) bubble columns requires good gas–liquid contacting whereby often gas flows as a discontinuous phase rising in the form of bubbles through a continuous liquid or slurry phase. From a practical viewpoint, the dispersed phase and corresponding rise velocity, by being sensitive to buoyancy, could be strongly impacted by the sea swells that ceaselessly assault FPSO units. To the best of the authors' knowledge, despite the growing significance of petroleum FPSO applications and potential on-board installation of multiphase reactors, investigations on flow dynamics of floating bubble columns is a virgin field of research. There are a few studies in the literature, which exclusively tackled hydrodynamic issues arising from static inclined bubble columns [9,10]. So far, only floating packed beds and fluidized beds received somewhat more coverage. Indeed, inclined configurations are increasingly studied in terms of flow behavior and phase maldistribution in packed and fluidized beds [11–17]. Other studies were interested on emulating fluidized beds under rolling motion with relevance to marine use [18–24], though disregarding the impact of other ship-motion degrees of freedom such as surge, sway and heave (translations), and pitch and yaw (rotations).

For the sake of providing additional knowledge in this emerging area of multiphase flows and reactors, the present study's object of scrutiny consisted of a liquid-batch bubble column operated in the homogeneous bubble flow regime and embarked on a hexapod ship motion simulator, which was submitted to a variety of motion regimes. Single sinusoidal excitations of roll,

* Corresponding author.

E-mail address: Faiçal.Larachi@gch.ulaval.ca (F. Larachi).

sway, heave, yaw and coupled sinusoidal excitations of roll+pitch were tested and a dual capacitance wire-mesh sensor inserted in the bubble column was employed to measure on-line the local void fraction and axial gas velocity. This wire mesh sensor technique, tested for the first time on a moving bubble column, enabled measurements in two-phase flows by sensing at high frequency and with millimeter spatial resolutions the local electrical capacitance in the vessel cross-wise planes. Post-processing algorithms thence enabled retrieving, after suitable calibration, the local void fractions, phase distributions, and with dual sensors, velocity hydrodynamic information. As a general tendency of the assessed column programmed motions, preliminary tests indicate a reduction of gas phase mean residence chiefly attributed to bubble upper-wall clustering and segregation foreshowing degradation of gas-liquid contacting of bubble columns onboard FPSO units.

2. Experimental

The moving bubble column assembly illustrated in Fig. 1 consisted of (1) a 5.7 cm inner-diameter and 170 cm high Plexiglas column equipped with (2) a flange-connectible dual 16×16 capacitance wire-mesh sensor (HZDR-Innovation GmbH, Dresden, Germany) to collect gas voidage, gas velocity and flow pattern information, while the whole of which was firmly upheld on (3) a 6-degree-of-freedom hexapod platform simulator (Symétrie, Nîmes, France) to emulate ship motion conditions.

Wire-mesh sensors belong to the realm of flow imaging techniques. Despite their intrusive character, they allow investigation of multiphase flows at high temporal resolutions. In addition, with their millimeter spatial resolution, they outperform their non-invasive direct rival techniques such as electrical capacitance

tomography [12]. Being electrical-field based, wire-mesh capacitance sensors enable measurement of the medium electrical permittivity in confinements between two planes of wire electrodes stretched through the flow cross-section [25–28]. In dual capacitance wire mesh sensors such as the one employed in this study, the two wire mesh modules were 12 mm apart (as illustrated from photo on the left of item (2) in Fig. 1 by the two blue plates) and were located 70 cm from the gas inlet (Fig. 1). Each wire-mesh sensor consisted of two orthogonally-arranged (upstream and downstream) planes, 1.5 mm afar, each made of 16 parallel stainless steel wires 0.4 mm in diameter. The upstream and downstream wire planes were, respectively, excited in transmission and reception modes. Such arrangement provided a spatially-resolved cross-sectional matrix of permittivity data composed of 148 full-square core pixels of $3.57 \times 3.57 \text{ mm}^2$ each and 40 peripheral area-reduced wall pixels for which only areal fractions inscribed within the flow region of interest were accounted for. The measuring technique gave access to a local multiphase mixture permittivity at each touchless nodal (cross-point) voxel stemming for the perpendicularly meeting transmission and reception wires (Fig. 1). To permit signal disambiguation of the excited nodal voxels, the sensor electronics briefly excited but one transmitting wire during a few μs with a high-frequency AC voltage while keeping all the other transmitting wires disabled at ground potential by means of a set of analog switches. The resulting AC currents established between the activated transmitter electrode and the receiving wire electrodes of the downstream plane were converted into proportional dc voltages detected in parallel by means of sensing blocks which include trans-impedance amplifiers, logarithmic demodulators and voltage amplifiers. The measured dc output voltages were related to the fluid electrical permittivity in the control volume surrounding each two-wire junction. A micro-controller was in charge of the analog switches and ADC timing.

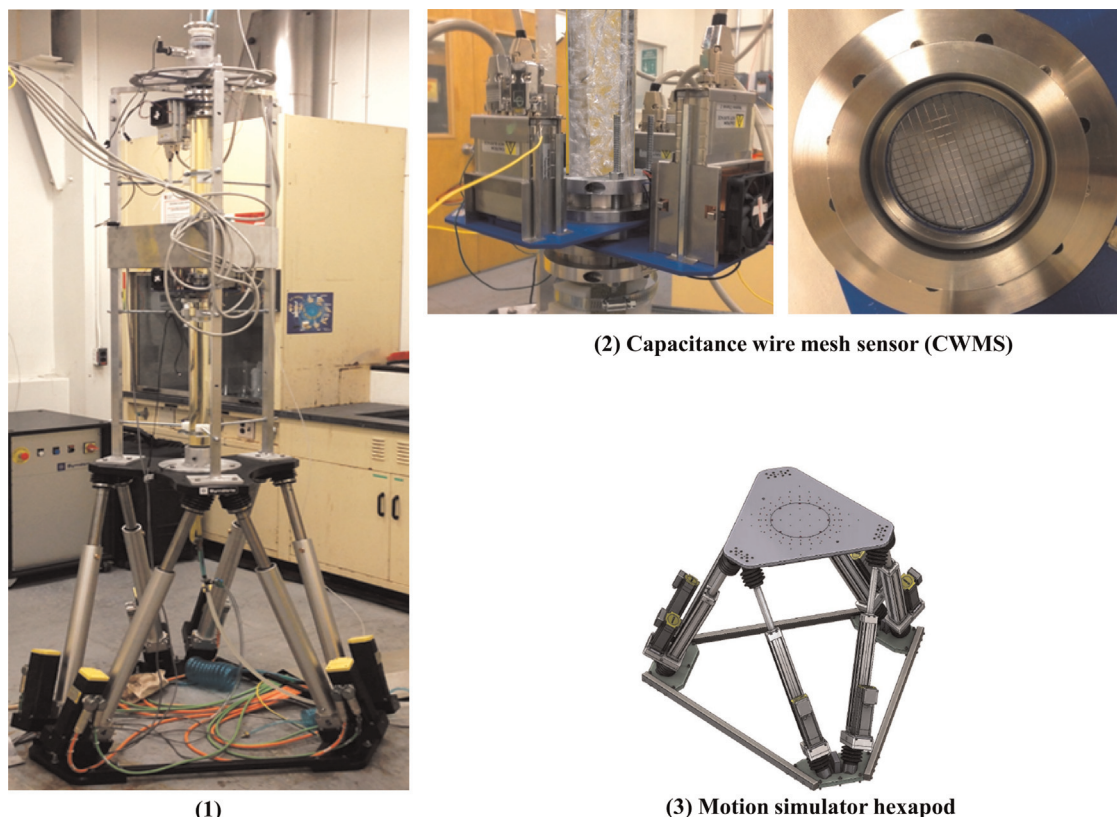


Fig. 1. Layout and components of the hexapod/wire-mesh sensor/bubble Plexiglas column assembly (1), capacitance wire-mesh sensor (2), and ship motion simulator (hexapod) (3). (For interpretation of the references to color in this figure, the reader is referred to the web version of this article.)

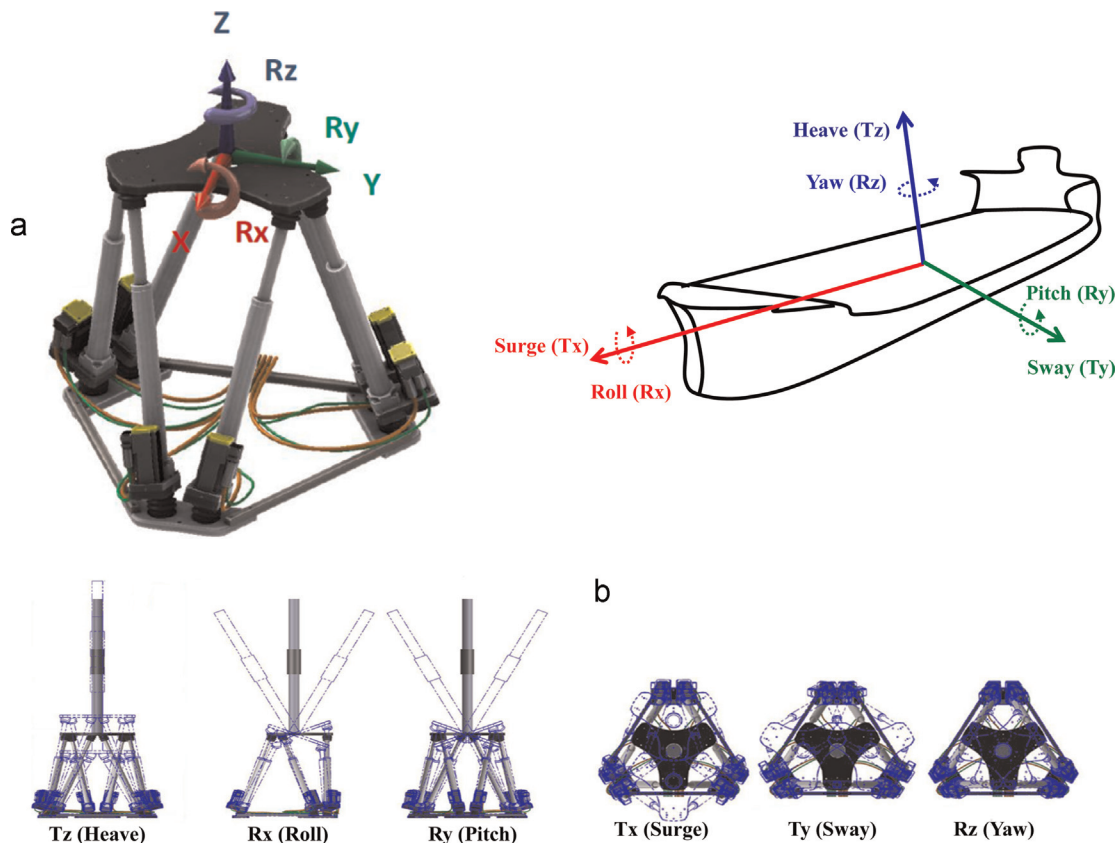


Fig. 2. (a) Ship motion simulator apparatus, (b) translation and rotation hexapod elementary (degree of freedom) motions.

Sweeping sequentially each individual transmitter wire allowed signal acquisition of all touchless cross-points over the entire column cross-section. More detailed descriptions on the wire-mesh sensor functionalities and data processing can be found elsewhere [29–31].

As depicted in Fig. 2, the hexapod platform was set to provide accurately the three translational (heave, along Z direction; surge, along X direction and sway, along Y direction) and three rotational (roll, around X axis; pitch, around Y axis and yaw, around Z axis) motions to mimic single-degree-of-freedom or composite dynamic displacements akin to those to be met on actual floating vessels. Apart from single-degree-of-freedom excitations, combined roll+pitch motions were tested in this work as well. Each rotation or translation motion of the hexapod platform was programmed for the present hydrodynamic study by generating sinusoidal motion paths given by: $p = A_p \sin(2\pi ft + \phi)$ with A_p the amplitude (mm for translation or degrees for rotation); f the frequency (Hz); t the elapsing time (s) and ϕ the phase lag (degrees). In addition to the effective duration of motions, a necessary softening delay of 5 s at the beginning and end of the motion sequence was added to reach the desired position, speed and acceleration, and return-to-zero position. For the particular instance of combined roll+pitch, a roll sinusoidal motion path (rotation around X axis) and pitch sinusoidal motion path (rotation around Y axis) were carried out with a 90° phase lag. All motions were sinusoidal excitations with frequencies 0.05, 0.1, 0.2 Hz to reflect those encountered in sea conditions [32,33]. These frequencies are compatible with the typical spectral frequency range corresponding to wind-generated fully developed sea conditions [32]. In addition, as shown in Journée and Massie [33], the frequency characteristics of heave and pitch motions in terms of heave and pitch transfer functions of crude oil carriers for stationary or forward-moving ship speed in deep water experiencing head and beam waves are coincident with our

hexapod tested range. The hexapod programmed motion parameters are summarized in Table 1.

Only the homogeneous bubbly flow regime was scrutinized in which air was sparged upwardly at a superficial velocity of 19 mm/s through a perforated distributor into liquid kerosene (density 789 kg/m³, viscosity 1.1 cp, surface tension 25.3 mN/m) filled upto 110 cm rest height in the column. This flow regime was first ascertained for the static vertical configuration of the column. Room temperature and atmospheric pressure prevailed in all the tests with the column maintained in static vertical and inclined postures as well as upon imposing the moving types described in Table 1. Upto 15 min stabilization time was necessary to ensure that the start-up transients had died out before data collection was triggered at a frame capture frequency of 100 Hz for 120 s. It is worthy of mention that the majority of bubbles produced with the distributor used in our study at the selected gas superficial velocity (befalling in the homogeneous bubble flow regime) had a diameter larger than the sensor mesh clearance. Visual observation led to an average bubble diameter ca. 4.5 mm representing, for a spherical bubble, a projected area 78% in excess of the mesh area.

Table 1
Tested motions and related characteristics.

Motion	Frequency (Hz)	Phase lag (deg.)	Amplitude (mm or deg.)
Roll (Rx)	0.05/0.1/0.2	0	15°
Roll (Rz) & Pitch (Ry)	0.05/0.1/0.2	90 for Rx & 0 for Ry	15° & 15°
Sway (Ty)	0.05/0.1/0.2	0	250 mm
Heave (Tz)	0.05/0.1/0.2	0	200 mm
Yaw (Rz)	0.05/0.1/0.2	0	15°

Therefore, the statistics of bubbles which might pass “unnoticed” through the wire mesh sensor was expected to be quite likely minor. However, in these conditions, there is no certainty that the invasive character of the wire mesh sensor would leave traceless the bubble column flows. The transit of bubbles, matter-of-factly, from lower to upper wire mesh planes of the dual sensor might not be neutral a travel and that coalescence and breakup phenomena may corrupt the genuine bubble trajectories and size distribution. Nevertheless, after testing air–water and air–kerosene systems, it was qualitatively inferred from wall observations that the bubble size was virtually unaffected by the presence of wire mesh sensor in the case of air–kerosene system unlike the air–water system. The reason remains unclear though it is believed that the fact that kerosene is a well-known coalescence-inhibiting liquid probably explains the stabilized gas–liquid interface and thus the indifference of bubble size to wire-like obstacles.

3. Data post-processing

The calibration methodology for gas holdup extraction was explained at great length in Da Silva et al. [29] reference which the interested readers may be directed to for more details. In summary, the log-linear transfer function parameters of each transmitter-receiver channel were estimated from the measured output voltages corresponding to single-phase low (air) and high (kerosene) permittivity calibration tests. Hence, calibration data were obtained for the two limiting cases of liquid-full and air-full columns which were assigned, respectively, 0% gas void fraction and 100% void fraction. These parameters were assumed to be primarily electronics specific and thus independent of the gas-liquid mixture present within the sensed nodal voxel. Once mapping these log-linear transfer function parameters was completed, changes in the output voltage associated with the presence of a gas-liquid mixture with varying volume fraction were isolated in terms of a two-phase electrical permittivity. Afterwards, a linear dependence between the measured permittivity thus-obtained

and the gas holdup was assumed. Precisely, this served to extract the pixel-affixed gas holdups – with the required areal re-normalization for the truncated wall-residing pixels – from the local mixture permittivity arising in two-phase flow in the neighborhood of each excited nodal voxel.

Bubble identification and thus determination of the bubble size distribution would have required dedicated interface recognition algorithms and signal post-processing procedures to accurately single out and recognize, among void fraction data, events corresponding to regions of connected gas-containing elements that are embedded within liquid-containing elements. However, no attempt was made in this study to develop such a methodology. Instead, an easier and direct representation of gas holdup time series was adopted as explained as follows. The pixel-affixed gas holdup (or void fraction) time series were gathered in the form of three-dimensional matrix $\alpha(x,y,t)$ which can be plotted in various manners to highlight the flow features arising in response to the hexapod movements. 2-D (Y,t) Euler slices with temporal visualization of the hydrodynamic behavior over the column cross-section were constructed after holdup line-averaging along a pre-selected X-direction (Fig. 3a,b). As symmetry loss of the flow structure along X-axis could be more or less tarnished after holdup line-averaging, 3-D Euler representations may prove more informative. Hence, 3-D visualizations of liquid-rich and gas-rich regions were elaborated using Matlab[®] iso-surface function reconstruction from the acquired (x,y,t) instantaneous gas holdup data with a defined threshold of 45% (Fig. 3b). These 3-D visualizations, in fact 2-D geometrical transverse fields evolved as a function of time (vertical axis), may prove very instructive in portraying instantaneous crosswise structures in the gas-liquid flow. Contrary to first impression, the grained structures popping up with time should certainly not be confounded with rising bubbles as the structures shown in Fig. 3b are Eulerian representations stemming from gas holdup times series the threshold of which only allows to distinguish between liquid-rich and gas-rich regions in the flow.

Besides the structural information captured in the form of local

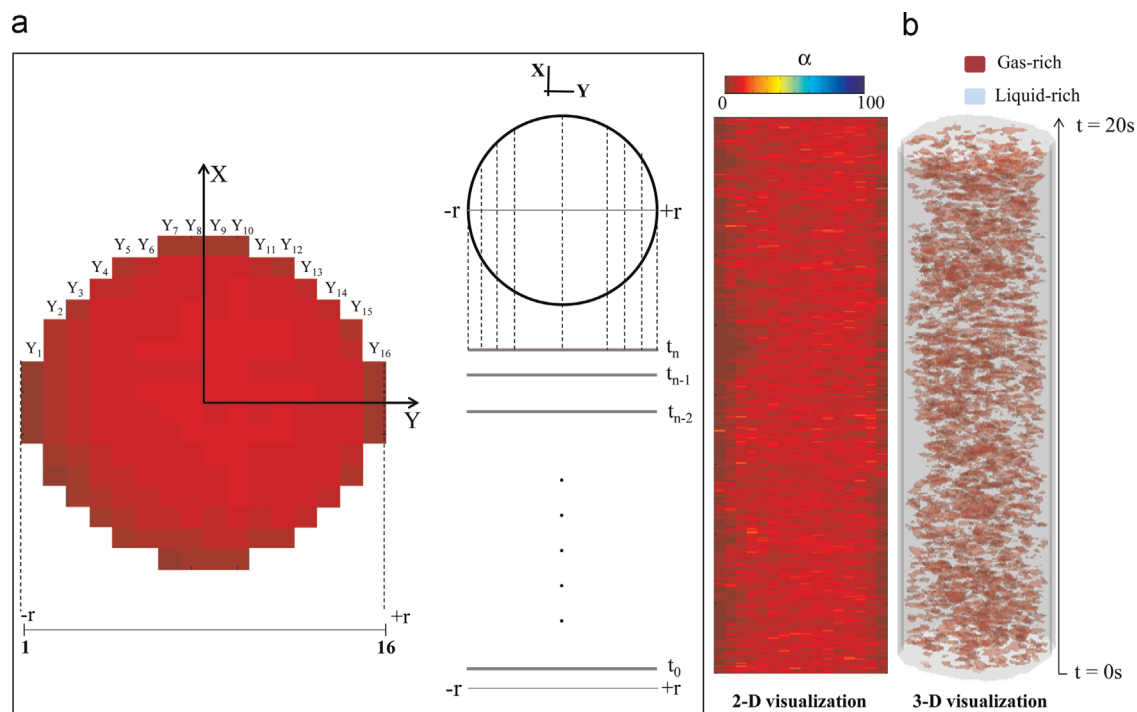


Fig. 3. Data processing and visualization procedure. (a) Line-averaging as a preamble to Euler slice temporal visualization (b) 2-D (Euler slice) visualization of (void-fraction) (a) and 3-D iso-surface visualization of gas-rich and liquid-rich presence for the stationary and vertical bubble column.

instantaneous gas holdups, gas holdup time series acquired at each plane of the dual wire mesh sensor proved instrumental in the determination of gas velocities. Such velocities, rather than to be conceived as local bubble rise velocities, should instead be viewed as estimations of the local streamwise (i.e., axial) time-averaged gas velocities, v_{zg} . Hence, the local instantaneous gas holdup signals, $\alpha_{ij}^{(u)}(t)$ and $\alpha_{ij}^{(d)}(t)$, registered, respectively, from corresponding cells (ij) in upstream and downstream sensing planes were cross-correlated in a pairwise manner through the $2 \times (148 + 40)$ mesh points, whereas upper and lower signals were delayed by variable time shifts, τ

$$CC_{ij}(\tau) = \frac{\sum_k \alpha_{ij,k}^{(u)} \alpha_{ij,k+\tau}^{(d)}}{\sqrt{\sum_k \{\alpha_{ij,k}^{(u)}\}^2 \sum_k \{\alpha_{ij,k}^{(d)}\}^2}} \quad (1)$$

In this equation, $CC_{ij}(\tau)$ designates the cross-correlation function at time shift τ , $\alpha_{ij,k}^{(u)}$, $\alpha_{ij,k}^{(d)} = \alpha_{ij,k}^{(u)} - \langle \alpha_{ij}^{(u)} \rangle$ and $\langle \alpha_{ij}^{(u)} \rangle$ stand, respectively, for the fluctuating gas holdup component and the time-averaged gas holdup at upstream plane nodal voxel (ij) occurring at discrete time instant k . Correspondingly, $\alpha_{ij,k+\tau}^{(d)} = \alpha_{ij,k+\tau}^{(d)} - \langle \alpha_{ij}^{(d)} \rangle$ and $\langle \alpha_{ij}^{(d)} \rangle$ stand, respectively, for the fluctuating gas holdup component and the time-averaged gas holdup at downstream plane nodal voxel (ij) registered at discrete time instant $k + \tau$.

In the homogeneous bubbly flow regime under consideration in this study, it is straightforward to conceive that the gas holdup as a scalar property is transported, as a result of the ceaseless passage of bubbles, between the upstream and downstream sensing planes of the dual wire mesh sensor. Random and chaotic motions in the bubble column contribute to the spread of the cross-correlation function around a maximum. This maximum yields an estimate of the average transit time of the gas holdup time series over a total observational time window, here 120 s at frame capture frequency of 100 Hz. This transit time coincides with time delay τ_{\max} where the above cross-correlation culminates:

$$\tau_{\max} \mapsto \max[CC_{ij}(\tau)] \quad (2)$$

From the known axial distance, $L = 12$ mm, between the two

planes and τ_{\max} thus determined, a local streamwise time-average gas velocity, v_{zG} , was computed:

$$\langle v_{zG} \rangle = \frac{L}{\tau_{\max}} \quad (3)$$

In the above cross-correlation analysis, it is worthy of mention that interpretation of computed velocities, especially high velocities, is difficult as these correspond to events which cannot be differentiated from spurious events likely arising from rapid “dispersive” crisscrossing of the same wire-mesh plane by the same bubbles.

4. Results and discussion

4.1. Static column

Visualizations in the form of 3-D Euler representations of gas and liquid instantaneous occupancies and 2-D instantaneous gas fraction averaged along the X-axis are presented in Fig. 4a₁–a₄ as a function of tilt angle for the static bubble column. A line-average representation was preferred over the commonly used azimuthal averaging on account of the axisymmetric breakup caused by vesper inclination. The resulting time-averaged holdup profiles are displayed in Fig. 4b₁–b₄. As depicted in the three representation sets for the static vertical column, the entire column cross-section was shared both by the liquid and air bubbles, expectably without signs of any phase segregation. Except a wall region predominantly occupied by the liquid, a relatively even distribution of gas prevailed in the rest of the column cross-section (Fig. 4a₁,b₁). This feature is in agreement with previous literature observations on void fraction distribution in bubbly flow regime at similar gas superficial velocity [34]. Inclining the column by 5, 10 and 15° resulted in the onset and development of permanent phase segregation leading to a breakdown of symmetry in phase distribution similar to the one reported for inclined packed or fluidized beds [11–16]. In column inclined positions, bubbles were forced to migrate toward the upper wall (U_w) region driven by buoyancy forces and accumulating into an increasingly slenderer bubbly layer as tilt angle was increased (Fig. 4a₂–a₄). Correspondingly, this

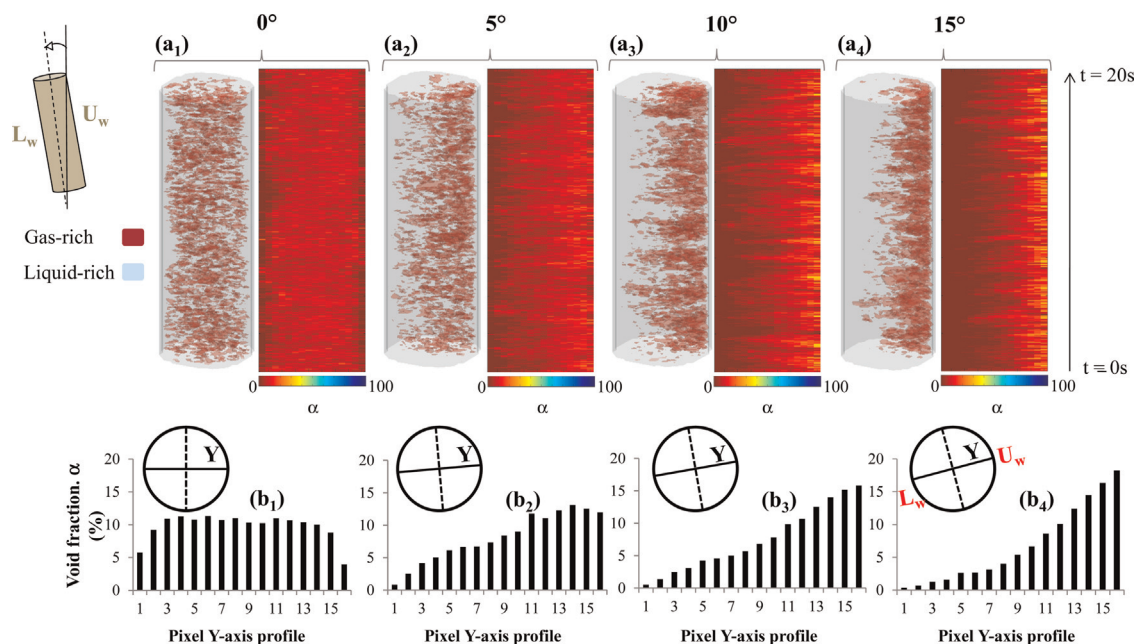


Fig. 4. Effect of bubble column tilt angle shown as (a) 3-D and 2-D Euler representations of gas-rich and liquid-rich presence and gas holdup (α) space-time distribution, respectively (b) pixel Y-axis profile of time- and line-averaged (along X direction) void fraction.

buoyancy driven gas flow resulted in a gradually gas-depleted lower wall (L_w) region evolving towards a liquid single-phase region with inclination angle (Fig. 4_b–4₄). The inception of inclination-triggered instabilities in bubble flow is discernible from the intermittent passages of gas-rich swarms in the form of shrinking–swelling structures as revealed from the 3-D Euler representations of Figs. 4_a₃,_a₄ probably due to the irregular downward liquid recirculation. Furthermore, the axisymmetric core–annulus gulf-stream structure known to occur in vertical vessel settings (Fig. 4_a₁,_b₁) due to liquid recirculation alongside the wall and bubble disengagement was supplanted by an asymmetric gross flow pattern once the column was inclined. Liquid towards the upper wall (U_w) region was driven in an upward manner by the bubble flow whereas due to progressive depletion of bubbles in the lower wall region (L_w), the liquid took a descending stride. It is worth noting that the gas holdup increases in the upper wall region from ca. 5% at 0° to almost 15% at 15°, which was not only the result of vessel inclination but also caused by the coalescence inhibition of bubbles characterizing kerosene–gas systems. These systems are known for their stabilized gas–liquid interface and tendency to foam [35].

Local streamwise time-average gas (interstitial) velocities were computed as described earlier from the average flight-time determination. Shown in Fig. 5_a₁–_a₄ are contour plots of local streamwise gas velocities as a function of vessel inclination. Gas velocity in the upper-wall region increased with increasing vessel tilt angle thus reinforcing the liquid bulk circulation [10]. It can also be seen in Fig. 5_a₂–_a₄ that a few pixels pertaining to the lower-wall column displayed abnormally large gas velocities (pixels in black color). Belonging to pixels located in the gas-depleted lower regions (L_w , Fig. 4_a₂–_a₄), such large rise velocities were attributed to spurious events resulting from the short-lived incursions/excursions of a few bubbles back and forth across the wire-mesh plane. Because of misleadingly shortening the computed flight time, the inflated velocities occurring in the lower-wall liquid-rich region were ignored in our analysis. Therefore, to make sense of the global effects of inclination on bubble motion, gas velocity density functions were plotted in Fig. 5_b. For the vertical column, gas interstitial velocities varied between ca. 4 cm/s for the slow-paced ones alongside the vessel walls and 25 cm/s

for those contributing to the fast traffic in the bubble column core. Inclining the column by 5, 10 and 15° shifted correspondingly the velocity distribution towards higher velocity modes, even featuring bimodality at the highest tested inclination, confirming correspondingly accelerated bubble traffic flow in the upper-wall region of the column.

4.2. Moving column

The bubble flow behavior as influenced by the column movements imposed via the hexapod programmed roll oscillations defined in Table 1 was examined next. 2-D and 3-D visualizations of the gas–liquid patterns in a column subjected to 3 different roll frequencies are illustrated in Fig. 6_a₂–_a₄. The gas–liquid pattern for the static vertical column was also shown for comparison (Fig. 6_a₁). Bubble motion under roll oscillations diverged remarkably from that prevailing in the static configuration. Bubbles were driven in a transverse zigzag choreography under roll oscillations distinctly differing from the nearly vertical trajectories observed in the static vertical posture. By being permanently compelled to track an evanescent upper-wall region, the migration of bubbles kept fast enough to match with the column tilting frequency which, as a result, governed the wall-to-wall bubble migration (Fig. 6_a₂–_a₄).

Contour plots of local streamwise time-average gas (interstitial) velocities corresponding to the 3 roll frequencies are presented in Fig. 6_b₂–_b₄. Two diametrically opposed regions bearing the fastest bubble rise events developed in the direction of vessel inclination (Fig. 6_b₂–_b₄). This was unlike the single-sided upper region with bubble flow prevalence as observed for the static inclined columns (Fig. 5_a₂–_a₄). These bubble-active regions grew in importance towards the column center with a decrease of roll frequency though featuring a tendency of diminishing velocity amplitude. A reduction in roll frequency was believed to slowdown the motion of bubbles toward the wall. This reduced by the same account the number of bubbles effectively reaching the upper wall region. Both effects contributed in mitigating the extent of liquid recirculation and correlatively the gas interstitial velocities. Gas velocity density functions corresponding to the tested roll motions are shown in Fig. 6_c. Vessel rolling clearly sped up gas interstitial velocity as

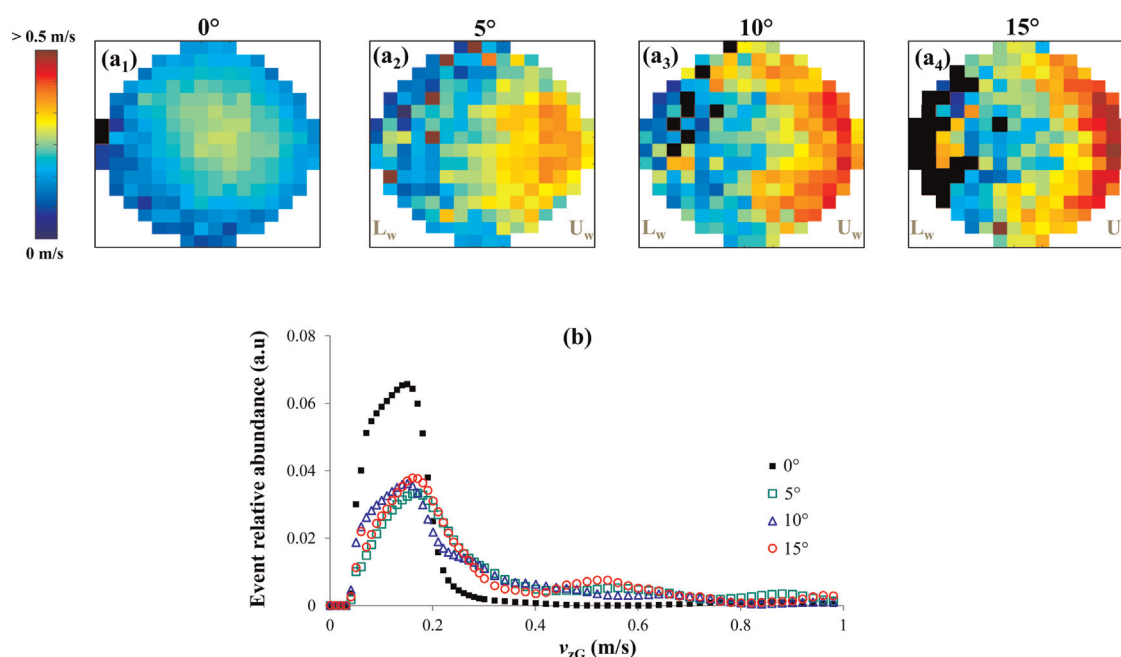


Fig. 5. Contour plots of local streamwise time-average gas velocities (a) and corresponding gas velocity density functions (b) as a function of column inclination.

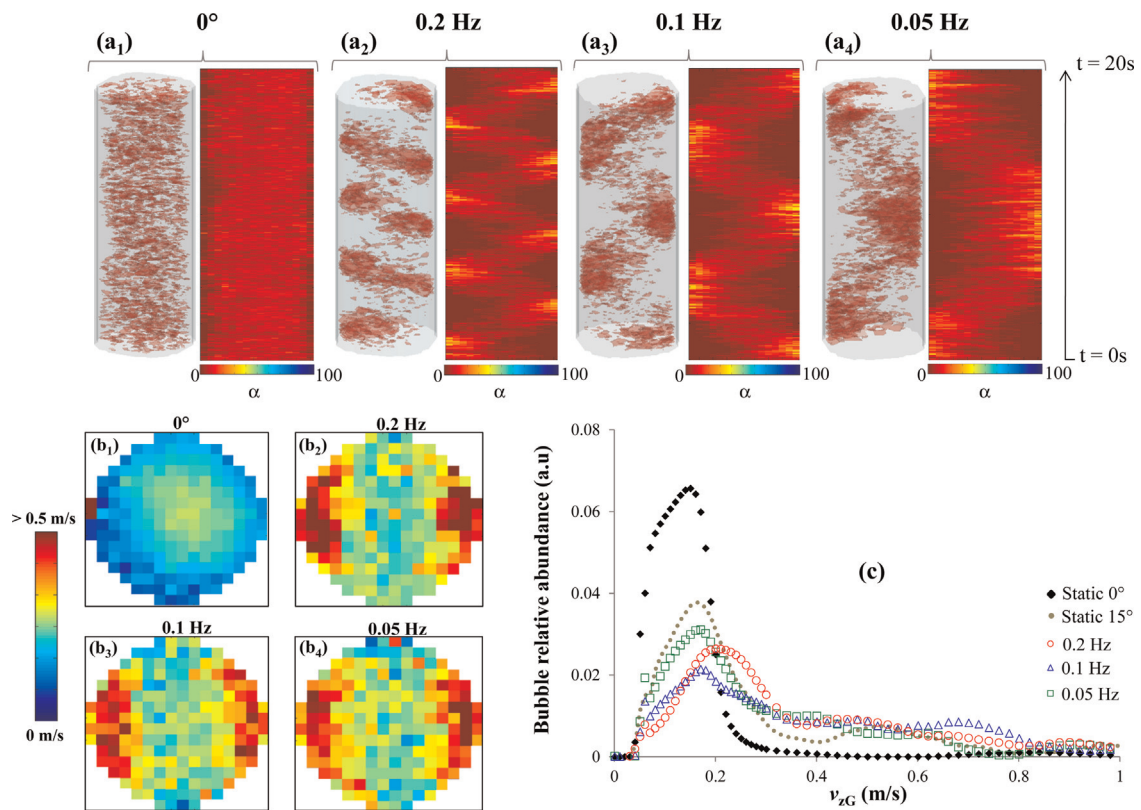


Fig. 6. 3-D and 2-D Euler representations of gas-rich and liquid-rich presence and gas holdup (α) space-time distribution, respectively (a), contour plots of local streamwise time-average gas velocities (b), corresponding gas velocity density functions (c) as a function of bubble column roll frequency (see Table 1).

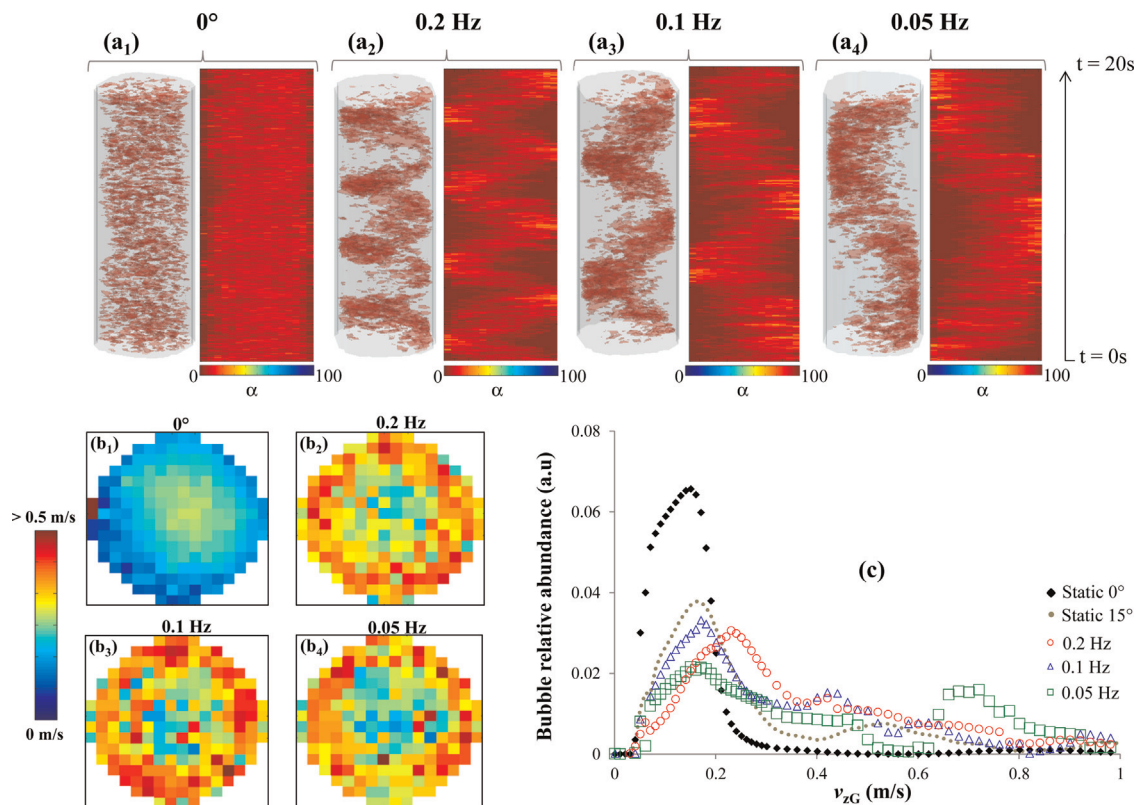


Fig. 7. 3-D and 2-D Euler representations of gas-rich and liquid-rich presence and gas holdup (α) space-time distribution, respectively (a), contour plots of local streamwise time-average gas velocities (b), corresponding gas velocity density functions (c) as a function of bubble column roll+pitch frequency (see Table 1).

compared to the static inclined configuration. The incidence of roll motion by extension to floating treatment units is expected to reflect in an undesirable reduction of gas-phase mean residence time.

Superimposed roll+pitch motion revealed greater irregularities in the gas–liquid flow patterns as exemplified in the 2-D and 3-D visualizations in Fig. 7a₂–a₄. It should be noted that the alternating takeover of roll and pitch motions due to the 90° phase lag (Table 1) imposed vessel positioning to be constantly inclined at 15° while rotating around a central vertical axis. Akin to the above discussed observations for the inclined static cases, vessel inclination prompted bubbles to buildup in the upper-wall region, while vessel rotation around the vertical axis induced an evident bubble swirling motion (Fig. 7a₂–a₄). Besides, the frequency increase in roll+pitch motion resulted in thinner spring-like gas-rich spiral arrangements developing, hand in hand, with an intensified liquid recirculation. The contour plots of local streamwise time-average gas (interstitial) velocities corresponding to roll+pitch excitation at the same three frequencies exposed ring-shaped fast (rising) interstitial gas velocities alongside the wall as illustrated in Fig. 7b₂–b₄. This comes in support of the bubbles quasi-exclusive displacement along the upper-wall region while remaining indifferent to the alternating takeover of roll and pitch motions. Shown in Fig. 7c are the gas velocity density functions corresponding to roll+pitch motion. The fact that the vessel was permanently inclined by 15° and stirred by the swirling upward motion of bubbles led to enhanced (rising) interstitial gas velocities exceeding largely those observed under the static 15°-inclination configuration.

The sway motion, unlike the roll and roll+pitch cases, affected the gas flow behavior in a less impressive manner as confirmed upon examination of the 2-D and 3-D visualizations shown in Fig. 8a₂–a₄. It can be observed that the bubble behavior under low sway frequencies (Fig. 8a₃,a₄) was qualitatively similar to the one manifesting in the case of the static vertical column (Fig. 8a₁). This

was unlike the higher frequency sway motion at 0.2 Hz, which altered the homogeneous bubbly flow by virtue of the inertial forces induced on kerosene displacements from +Y to -Y at the precise moments when the sway motion came to reach its half-period halts. The resulting zigzag-like displacements of the gas-rich structures from +Y to -Y and then from -Y to +Y were effects measurable by means of the wire-mesh sensor as shown in Fig. 8a₂. The consecutive displacement and collision of liquid bulk flow on the walls resulted in bubbles partially clustering and displacing toward the opposite walls thereby enhancing liquid circulation and (rising) interstitial gas velocities. The contour plots of local streamwise time-average gas (interstitial) velocities corresponding to sway motion at three frequencies are illustrated in Fig. 8b₂–b₄. In particular, a two-zone bubble clustering nearby the walls was clearly distinguishable for the highest frequency in Fig. 8b₂. However, this structure was different from the bubble-active regions identified earlier under inclined, roll, and roll+pitch cases (Figs. 5a₂–a₄, 6 b₂–b₄ and 7 b₂–b₄). From Fig. 8c, one can observe that the gas velocity density functions in the static vertical column as well as for those corresponding to low-frequency sway motion (0.05 and 0.1 Hz) were quite the same with gas interstitial velocities in the 4–23 cm/s range, while under high-frequency sway (0.2 Hz), gas interstitial velocities could be as high as 30 cm/s.

Finally, the incidence on the bubbly flow pattern of yaw and heave motions and their frequencies was captured in the 2-D and 3-D visualizations presented in Fig. 9a₂–a₄. Heave corresponding to piston-like vertical vibrations and yaw constraining column rotational oscillations around its revolution axis (Fig. 2) regardless of frequency were virtually impactless in terms of gas–liquid flow behavior, whose features were reminiscent of those of the stationary vertical column posture (Fig. 9a₁). This is confirmed from the contour plots of time-averaged local streamwise time-average gas velocities for the 4 instances (Fig. 9b₁–b₄). Visibly too low for the imposed frequencies to bring about noticeable flow alterations,

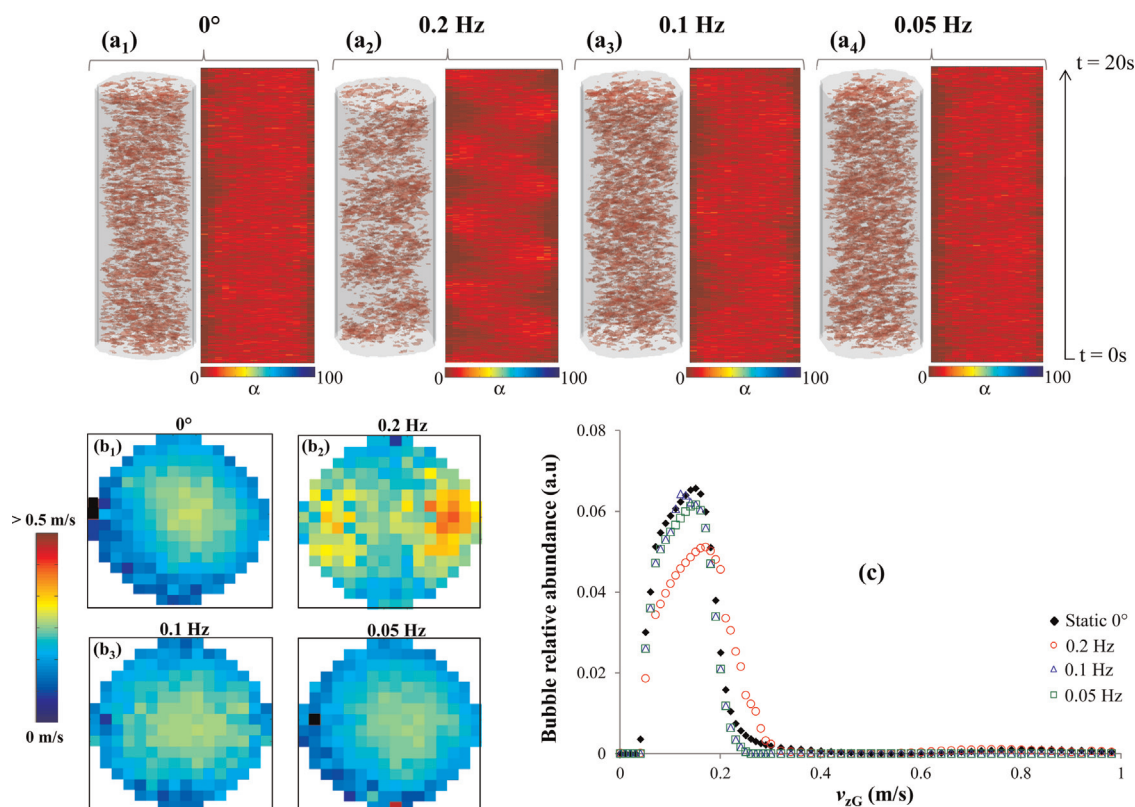


Fig. 8. 3-D and 2-D Euler representations of gas-rich and liquid-rich presence and gas holdup (α) space-time distribution, respectively (a), contour plots of local streamwise time-average gas velocities (b), corresponding gas velocity density functions (c) as a function of bubble column sway frequency (see Table 1).

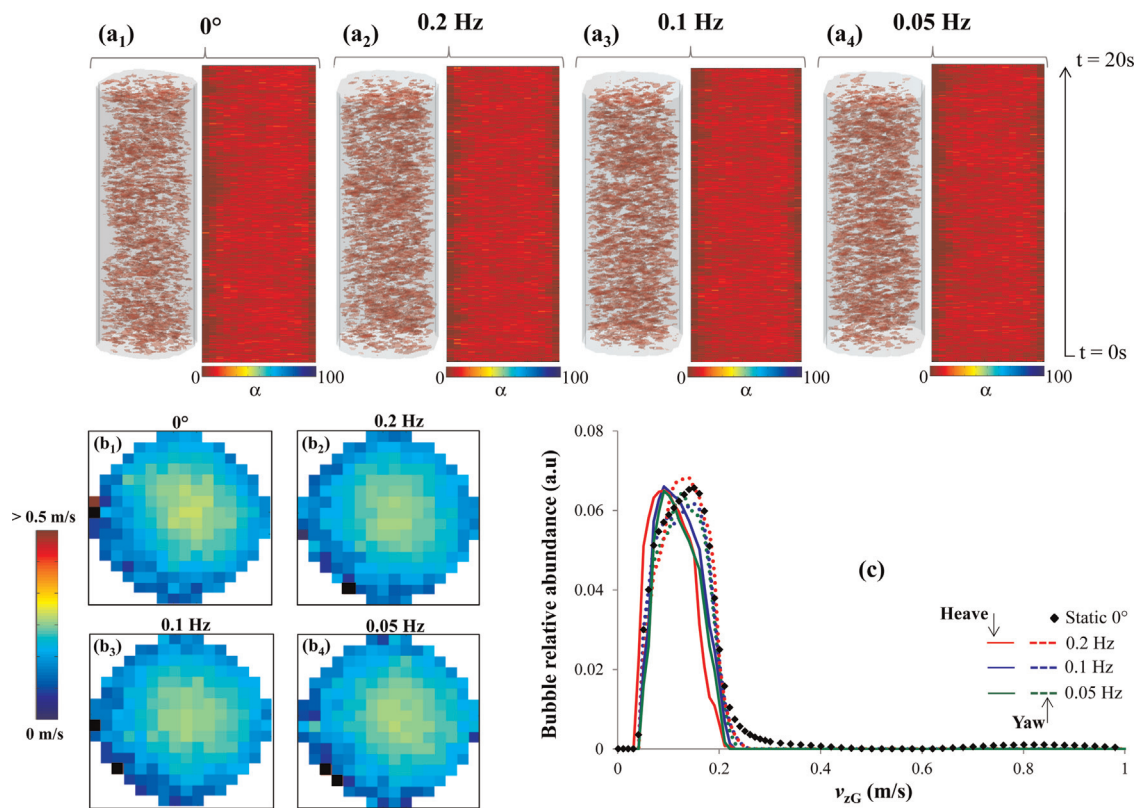


Fig. 9. 3-D and 2-D Euler representations of gas-rich and liquid-rich presence and gas holdup (α) space-time distribution, respectively (a), contour plots of local streamwise time-average gas velocities (b), corresponding gas velocity density functions (c) as a function of bubble column heave and yaw frequencies (see Table 1).

the inertial forces played a minor role hence barely affecting the liquid recirculation patterns. Yet, the gas velocity density functions presented in Fig. 9c indicated in the case of heave motion a loss in high-velocity events as compared to that of the static vertical column. The heave-controlled artificial axial back-mixing prompted by antagonistic ascending and descending liquid bulk movements is believed to be responsible for smoothing out the highest gas interstitial velocities.

5. Conclusion

The bubble flow behavior was monitored in a liquid-batch bubble column subject to artificial sea conditions emulated using a computer-controlled six-degree-of-freedom robot by means of a flange-inserted dual capacitance wire-mesh sensor. Sinusoidal excitations from single and paired degree(s) of freedom, namely, translations (surge or sway, heave) and rotations (roll or pitch, yaw, roll+pitch) in the 0.05–0.2 Hz frequency range were applied to the bubble column, via an hexapod ship motion simulator, to gain insights on the impact of sea swells on the hydrodynamic response of offshore bubble column units. A dual capacitance wire-mesh sensor was used to provide some preliminary results on the measurement of local void fraction and gas interstitial velocities and on the qualitative flow pattern changes induced by the various vessel motions.

As a general tendency of interrogated vessel motions, preliminary tests indicate a reduction of gas phase mean residence attributed to bubble clustering and segregation, which foreshows degradation of gas–liquid contacting in bubble columns onboard FPSO units. Specifically, roll and roll+pitch excitations induced phase segregation within the column showcasing bubbles, respectively, zigzagging and swirling in a commensurate manner with the imposed motion frequency. Bubble displacements and

buildup at the successive vessel upper-wall regions strengthened liquid recirculation and promoted larger gas interstitial velocities. For the horizontal translational (sway) movements induced by high frequency (0.2 Hz), inertial forces were strong enough to periodically translocate liquid resulting in zigzag-like bubble displacements and bubble clustering nearby the walls. A notable effect also took place at heave high-frequency reflecting in an artificial back-mixing, the tendency of which was to slowdown the fastest bubbles. It can be inferred from these hexapod emulated oscillations, that vessel motion will affect the performances of offshore bubble column treatment units. Future works will therefore be directed toward how column-movement hydrodynamics will impact mass transfer characteristics such as gas–liquid interfacial area and volumetric mass transfer coefficients.

Finally, high-velocity spurious events resulting from short-lived incursions/excursions of a few bubbles back and forth across the wire-mesh plane were difficult to distinguish from events corresponding to actual large gas interstitial velocities. This was due to the separation distance between the two wire mesh modules which was not optimized in the present dual wire mesh sensor configuration. To avert such limitation in future designs, it is recommended that the inter-module distance is optimized as a function of bubble sizes to allow accurate and quantitative assessment of gas velocities in stationary and moving bubble columns.

Acknowledgments

The authors gratefully acknowledge the Natural Sciences and Engineering Research Council of Canada and the Canada Research Chairs on Sustainable Energy Processes and Materials for their financial support.

Appendix A. Supplementary material

Supplementary data associated with this article can be found in the online version at <http://dx.doi.org/10.1016/j.flowmeasinst.2015.07.012>.

References

- [1] N. Kantarci, F. Borak, K.O. Ulgen, Bubble column reactors (Review), *Process Biochem.* 40 (2005) 2263–2283.
- [2] B.C. Gandhi, Hydrodynamic studies in a slurry bubble column, Masters of Engineering Science thesis, The University of Western Ontario, 1997.
- [3] L.S. Fan, *Gas–Liquid–Solid Fluidization*, Butterworths, Boston, 1989.
- [4] M.P. Dudukovic, N. Devanathan, Bubble column reactors: some recent developments, in: H.I. de Lasa, G. Dogu, A. Ravella (Eds.), *Chemical Reactor Technology for Environmentally Safe Reactors and Products*. Nato-ASI Symposium Series, Vol. 225, Kluwer Academic Publishers, 1992, pp. 353–377.
- [5] J.J. Lewnard, T.H. Hsiung, J.F. White, D.M. Brown, Single-step Synthesis of Dimethyl Ether in a Slurry Reactor, *Chem. Eng. Sci.* 45 (8) (1990) 2735–2741.
- [6] W.L. Leffler, R. Pattarozzi, G. Sterling, A century getting ready, in: W.L. Leffler, R. Pattarozzi, G. Sterling (Eds.), 2nd edition, PennWell Books, Tulsa, Oklahoma, 2011, pp. 1–30.
- [7] International energy agency, World energy outlook 2010. (www.worldenergyoutlook.org/publications/weo-2010/).
- [8] Offshore magazine, deepwater solutions & records for concept selection: going deeper with production technology, 2012, p.72 (www.offshore-mag.com).
- [9] C.L. Hudson, Effect of inclination on hydrodynamics in bubble columns and fluidized beds, Digitized Theses Paper 2701 1996.
- [10] G.Z. Lu, K. Bittorf, B.G. Thompson, M.R. Gray, Liquid circulation and mixing in an inclined bubble column, *Can. J. Chem. Eng.* 75 (2) (1997) 290–298.
- [11] A. Atta, M. Schubert, K. Nigam, S. Roy, F. Larachi, Co-current descending two-phase flows in inclined packed beds: experiments versus simulations, *Can. J. Chem. Eng.* 88 (5) (2010) 742–750.
- [12] M. Schubert, M. Hamidipour, C. Duchesne, F. Larachi, Hydrodynamics of co-current two phase flows in slanted porous media—modulation of pulse flow via bed obliquity, *AIChE J.* 56 (12) (2010) 3189–3205.
- [13] H. Bouteldja, M. Hamidipour, F. Larachi, Hydrodynamics of an inclined gas–liquid concurrent upflow packed bed, *Chem. Eng. Sci.* 102 (11) (2013) 397–404.
- [14] D. O’Dea, V. Rudolph, Y. Chong, L. Leung, The effect of inclination on fluidized beds, *Powder Technol.* 63 (2) (1990) 169–178.
- [15] J. Valverde, A. Castellanos, M. Quintanilla, F. Gilabert, Effect of inclination on gas-fluidized beds of fine cohesive powders, *Powder Technol.* 182 (3) (2008) 398–405.
- [16] C. Hudson, C. Briens, A. Prakash, Effect of inclination on liquid–solid fluidized beds, *Powder Technol.* 89 (2) (1996) 101–113.
- [17] B. Yakubov, J. Tanny, D.M. Maron, N. Brauner, The dynamics and structure of a liquid–solid fluidized bed in inclined pipes, *Chem. Eng. J.* 128 (2) (2007) 105–114.
- [18] T. Nakanishi, S. Nakai, T. Kadota, T. Furukawa, S. Inoue, Y. Wakiyama, A. Yamada, Experiments on performance of fluidized bed for marine use, *J. Mar. Eng. Soc. Jpn.* 14 (9) (1979) 808–819.
- [19] S. Namie, T. Osanai, H. Yamanouchi, T. Yokomura, Investigation on fluidized bed combustion for marine application, *J. Mar. Eng. Soc. Jpn.* 19 (12) (1984) 943–950.
- [20] H. Murata, H. Oka, M. Adachi, K. Harumi, Effects of the ship motion on gas–solid flow and heat transfer in a circulating fluidized bed, *Powder Technol.* 231 (2012) 7–17.
- [21] T. Zhao, K. Liu, H. Murata, K. Harumi, M. Takei, Investigation of bed-to-wall heat transfer characteristics in a rolling circulating fluidized bed, *Powder Technol.* 269 (2015) 46–54.
- [22] W. Zeiczak, Investigation of fluidized bed of the physical model of the marine fluidized bed boiler, *J. Polish CIMAC* 3 (1) (2008) 183–190.
- [23] T. Yasui, T. Nakayama, K. Yoshida, Heat transfer characteristics in a rocking fluidized bed, *Int. J. Heat Mass Transf.* 11 (5) (1984) 477–488.
- [24] T. Zhao, K. Liu, H. Murata, K. Harumi, M. Takei, Experimental and numerical investigation of particle distribution behaviors in a rolling circulating fluidized bed, *Powder Technol.* 258 (2014) 38–48.
- [25] E. Schleicher, T. Aydin, C. Torres, E. Pereyra, C. Sarica, U. Hampel, Refined reconstruction of liquid–gas interface structures for oil–gas stratified two-phase flow using wire-mesh sensor, in: Proceedings of the 5th International Workshop on Process Tomography, Jeju, South Korea, 2014.
- [26] M. Schubert, A. Khetan, M.J. Da Silva, H. Kryk, Spatially resolved inline measurement of liquid velocity in TBRs, *Chem. Eng. J.* 158 (3) (2010) 623–632.
- [27] M.J. Da Silva, E. Schleicher, U. Hampel, Capacitance wire-mesh sensor for fast measurement of phase fraction distribution, *Meas. Sci. Technol.* 18 (7) (2007) 2245–2251.
- [28] L. Szalinski, L.A. Abdulkareem, M.J. Da Silva, S. Thiele, M. Beyer, D. Lucas, V. Hernandez Perez, U. Hampel, B.J. Azzopardi, Comparative study of gas–oil and gas–water two-phase flow in a vertical pipe, *Chem. Eng. Sci.* 65 (2010) 3836–3848.
- [29] M.J. Da Silva, S. Thiele, L. Abdulkareem, B.J. Azzopardi, U. Hampel, High-resolution gas–oil two-phase flow visualization with a capacitance wire-mesh sensor, *Flow Meas. Inst.* 21 (2010) 191–197.
- [30] J.-D. Llamas, C. Perat, F. Lesage, M. Weber, U. D’Ortona, G. Wild, Wire mesh tomography applied to trickle beds: a new way to study liquid maldistribution, *Chem. Eng. Process.* 47 (2008) 1765–1770.
- [31] U. Hampel, J. Otahal, S. Boden, M. Beyer, E. Schleicher, W. Zimmermann, M. Jicha, Miniature conductivity wire-mesh sensor for gas–liquid two-phase flow measurement, *Flow Meas. Inst.* 20 (2009) 15–21.
- [32] J. Moskowitz, Estimates of the power spectrum for fully developed seas for wind speeds of 20 to 40 knots, *J. Geophys. Res.* 69 (24) (1964) 5161–5179.
- [33] J. Journée, W. Massie, *Offshore hydromechanics*, Delft University of Technology, Delft, The Netherlands, 2001. Available from: (<http://www.shipmotions.nl/DUT/LectureNotes>).
- [34] M.T. Dhotre, J.B. Joshi, Two-dimensional CFD model for the prediction of flow pattern, pressure drop and heat transfer coefficient in bubble column reactors, *Chem. Eng. Res. Des.* 82 (6) (2004) 689–707.
- [35] H. Roques, Y. Aurelle, M. Aoudjehane, N. Siem, J. Rabat, Etude expérimentale des phénomènes de coalescence dans les systèmes bulles-gouttes (Experimental study of coalescence phenomena in bubble-drop systems), *Oil Gas Sci. Technol.-Rev. IFP* 42 (2) (1987) 163–177.